

Theory of Myelin Coiling

Jung-Ren Huang*

James Franck Institute and Department of Physics, University of Chicago
5640 S. Ellis Avenue, Chicago, Illinois 60637

August 31, 2018

Abstract. A new model is proposed to explain coiling of myelins composed of fluid bilayers. This model allows the constituent bilayer cylinders of a myelin to be non-coaxial and the bilayer lateral tension to vary from bilayer to bilayer. The calculations show that a myelin would bend or coil to lower its free energy when the bilayer lateral tension is sufficiently large. From a mechanical point of view, the proposed coiling mechanism is analogous to the classical Euler buckling of a thin elastic rod under axial compression. The analysis of a simple two-bilayer case suggests that a bilayer lateral tension of about 1 dyne/cm can easily induce coiling of myelins of typical lipid bilayers. This model signifies the importance of bilayer lateral tension in determining the morphology of myelinic structures.

PACS. 87.16.Dg Membranes, bilayers, and vesicles – 82.70.Uv Surfactants, micellar solutions, vesicles, lamellae, amphiphilic systems, etc. – 82.70.-y Disperse systems; complex fluids

1 Introduction

Surfactant molecules such as polar lipids self-assemble into fluid bilayers when dissolved in water at sufficiently high temperatures [1, 2]. If the surfactant concentration is large enough, bilayers stack to form multilayer structures called lamellae or multilamellae (L_α phase) [3]. In some experiments [4, 5, 6, 7, 8, 9], bilayers curve collectively to form nested cylindrical multilamellae known as myelin figures or simply, myelins (Fig. 1). Under certain conditions, myelins may bend to form coils or double helices [8, 10, 11, 12, 13, 14]. Because myelins have potential applications such as controlled drug delivery [15], detailed knowledge of their structure and behavior is desired. Recently, a geometrical model was proposed to account for formation of myelins [16]. This model suggests that if the inter-bilayer repulsion is large enough, a flat multilamella is unstable against myelin formation, i.e., it would transform into a myelin or myelins in order to lower its energy. In this paper we will focus on coiling of myelins composed of fluid bilayers and present a theory to explain why they coil.

Several theories of myelin coiling have been proposed. Lin et al. reported that the presence of enough Ca^{2+} ions led to coiling of the myelins of binary mixtures of cardiolipin and phosphatidylcholines [10]. Mishima and his co-workers studied the double helix formation of the myelins composed of egg-yolk phosphatidylcholine bilayers [12]. The authors of these two works attributed the

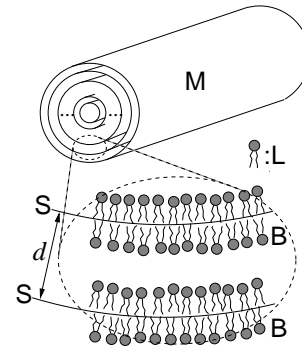


Figure 1: Sketch of myelin structure. Myelins (M) are multilamellar tubes composed of nested bilayer cylinders. Oval inset shows arrangements of surfactant molecules (L) in bilayers (B) [1, 2], where the mid-surface (S) of a bilayer separates the two opposing monolayers. The symbol d denotes the inter-bilayer spacing. In the upper drawing (M), only the bilayer mid-surfaces are shown. Typical value of bilayer thickness or inter-bilayer spacing is about several nanometers [1, 2] and that of myelin diameter ranges from a few micrometers to about 50 micrometers [5, 6, 7, 8, 9].

*email: jhuang2@uchicago.edu

observed coiling to surface adhesion. Frette et al. investigated coiling of the myelins of phospholipid bilayers in the presence of anchored polymers [13]. They suggested that coiling was due to a coupling between local bilayer curvature and polymer concentration. In addition to the above theories, Santangelo and Pincus proposed a myelin model and showed that myelins are unstable to coiling when the bilayer spontaneous curvature is nonzero or when the equilibrium inter-bilayer spacing is decreased [17]. Here we develop a new model. Our model allows the bilayer cylinders of a myelin to be non-coaxial and the bilayer tension to vary from bilayer to bilayer [18, 19]. By taking account of these two degrees of freedom, we will show that a sufficiently large bilayer tension may cause a myelin to coil. The coiling mechanism proposed here is similar to the classical Euler buckling of a thin elastic rod under axial load [20].

This paper is organized as follows. In Section 2 we describe the experimental observations that lead to our model. The proposed coiling mechanism is explained with a two-dimensional example in Section 3. The definition of our myelin coiling model is given in Section 4. We study coiling of a myelin composed of multiple bilayers in Section 5. Coiling of a two-bilayer myelin is investigated closely in Section 6. In Section 7 we discuss important features and implications of our model. Finally, Section 8 concludes our work.

2 Contact Experiment and Myelin Structure

In order to provide the motivation for this work, we will examine closely how myelins are created as well as their internal structure. We will show that the lateral tension of bilayers [18, 19] should be taken into consideration and moreover, the constituent bilayer cylinders of a myelin need not be concentric.

Myelins are multilamellar tubes composed of nested cylindrical fluid bilayers (Fig. 1). They are usually produced in contact experiments [6, 7, 8]: water is brought into contact with a lump of concentrated surfactant at temperatures high enough so that the bilayers are in fluid state. Upon contact myelins form at the interface and grow into water. The growth of myelins is roughly diffusion-like initially and slows down significantly after a few minutes [11, 14, 21]. While myelins are still growing, coiling of single myelins or double helix formation of two intertwisting myelins are often observed [11]. Experiments show that as myelins grow, water enters myelins mainly via the root region (Fig. 2a) [7, 8]. Thus, the influx of material, surfactant and water, that supports myelin growth comes from the back of myelins, i.e., the root region. Because the root region contains defects of sizes smaller than typical myelin diameters [21, 22], the material flux density for a growing

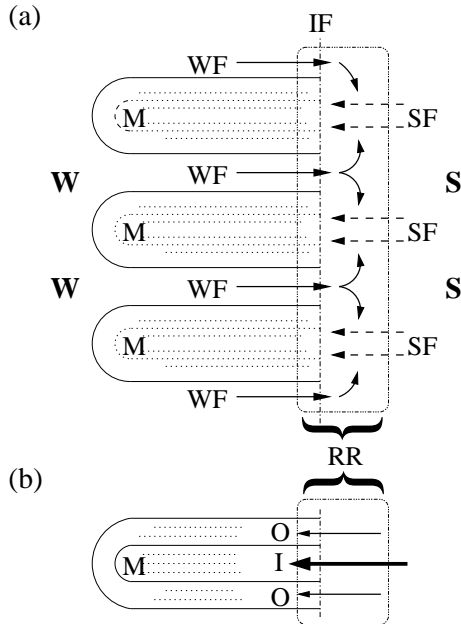


Figure 2: Sketch of myelin growth and material flux in a contact experiment. (a): Myelins (M) grow from the interface (IF) of water (W) and bulk surfactant (S). The water flux (WF) and surfactant flux (SF) supporting myelin growth enter myelins via the root region (RR). Solid and dash arrows indicate the directions of the water and surfactant fluxes, respectively [7, 8]. (b): A single myelin (M) is naively divided into a core (I) and a shell (O). As represented by the lengths of the respective arrows, the material flux densities for these two parts can be different. The bilayers of the shell would be in tension if the material flux density for the core is larger than that for the shell.

myelin is expected to be nonuniform¹. Figure 2b provides a simple and idealized example of nonuniform material influx density. In this example the myelin is arbitrarily divided into two parts, a core and a shell. The defect structure in the root region is such that the material flux density for the shell is less than that for the core, which implies that the shell is being stretched axially and the core compressed also axially. Therefore the bilayer tension is expected to be *nonuniform* and furthermore, the bilayers in the shell should be under tension. We note that the fluidity of a bilayer leads to a uniform tension throughout the bilayer. In contrast, the notion of “*nonuniform* tension” used in this work always means the tension may vary from bilayer to bilayer.

Intuitively the bilayer tension in a myelin composed of fluid bilayers should have some degree of nonuniformity, regardless of how the myelin is prepared. Like an air bubble in water, where the interfacial tension is balanced by a pressure difference across the air-water interface (Laplace’s formula), at least the outermost bilayer of a myelin should be under tension in order to cancel out the repulsion from the neighboring bilayer and thus maintain its cylindrical shape of the body and spherical shape of the end cap(s). If one or some of the bilayers are under tension, the force balance for the myelin body or the end cap(s) implies that the bilayer tension may be nonuniform, i.e., it may change from bilayer to bilayer.

From the above arguments we expect that the bilayer lateral tension can be variable not only from bilayer to bilayer but also from myelin to myelin. A general myelin model should take this degree of freedom into account. Myelins of uniform bilayer tension are just special cases of such a model. In addition, we will not presume the bilayer cylinders of a myelin to be concentric or coaxial since there is no reason to do so, especially for coiled myelins. Hence, the *eccentricities* of the bilayer cylinders appear in our myelin model naturally. We will show how these two variables, the bilayer lateral tension and cylinder eccentricity, can give rise to myelin coiling.

3 Bending of a Two-dimensional Tube

This section gives a detailed account of how an artificial two-dimensional tube can be unstable against bending, i.e., bending may reduce the tube’s free energy. Although myelin coiling occurs in three dimensions, this two-dimensional case, nevertheless, captures all the essential features of the myelin coiling model proposed in this work. Therefore, not only does this simple example offer a physical insight into why myelins coil, it also provides a frame-

¹The nonuniformity of the material flux density depends on the defect structure in the root region, which would evolve over time since defects are not energetically favorable.

work for modeling myelin coiling later in this paper. In the following we will first define the two-dimensional tube and specify how it deforms. Then we will show that the tube may indeed curve to lower its energy. The two-step deformation developed here makes it easy to determine changes in the energies.

3.1 Geometry and Two-step Deformation

Figure 3 describes the geometry of the two-dimensional tube and explains how it deforms. The tube comprises a core, **fc**, and a perimeter, **abde**, which are two-dimensional analogues of the inner and outer cylinders of the two-bilayer myelin studied in Section 6, respectively. All the state parameters, such as d_r , d_l and θ , are defined in the figure caption. The eccentricities of the bilayer cylinders in a myelin are simulated in this two-dimensional case by allowing the spacings d_l and d_r between the core and the perimeter to vary. The perimeter **abde** of length

$$L_{2D} \equiv L_l + L_c + L_r \quad (1)$$

is extensible and under uniform tension. The core **fc** exerts a force on the end cap **bd** to counterbalance the tension of the perimeter and prevent the tube from collapsing. For simplicity we assume the core to be of zero thickness and subject to bending only, i.e., its length L_m is constant. One may think of the core as a spring of infinite spring constant. Allowing L_m to vary amounts to reducing the spring constant to a finite value and thus adding one more degree of freedom to the system, which would not invalidate the conclusions of this section.

The tube area A_{2D} is postulated to be constant (Fig. 3):

$$\begin{aligned} A_{2D} &= 2d_0L_0 + \frac{\pi}{2}d_0^2 \cdot \hat{c} \\ &= \frac{\theta}{2} [(R + d_r)^2 - (R - d_l)^2] \\ &\quad + \frac{\pi}{2} \left(\frac{d_l + d_r}{2} \right)^2 \hat{c}, \end{aligned} \quad (2)$$

where the angle θ can be larger than 2π , i.e., the tube may coil, and $\hat{c} = 0$ or 1. The area conservation in two dimensions is analogous to the volume conservation in three dimensions (Sect. 4.3). In order to examine the effect of the end cap **bd**, we deliberately multiply every end cap contribution by the parameter \hat{c} . We will demonstrate that when the tube’s aspect ratio $L_0/2d_0$ is much greater than one, all the end cap contributions are negligible, i.e., we can set $\hat{c} = 0$.

The deformation of this two-dimensional tube takes place in two steps (Fig. 3): the tube is transformed from the initial state (i) into the intermediate state (ii) and then into the final state (iii). The initial tube is straight and its shape is symmetric with respect to the line **fc**. From state (i) to state (ii) the tube curves with fixed d_l ,

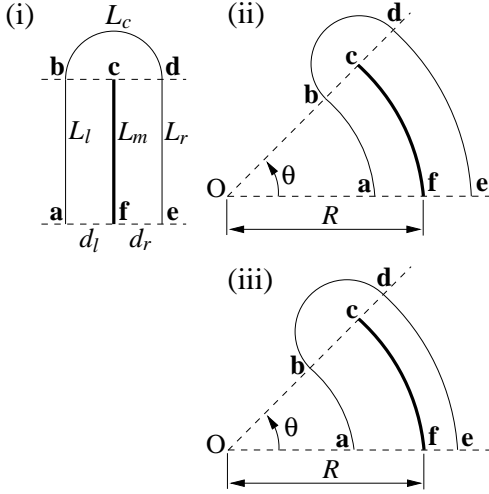


Figure 3: Two-step deformation of a two-dimensional tube. The tube is initially in state (i) and transforms into the intermediate state (ii) and then into the final state (iii). During the deformation the tube area is conserved. The tube consists of a core, **fc**, and a perimeter, **abde**. The core **fc** is of zero thickness and subject to bending only, i.e., its length is fixed. The perimeter **abde** is composed of two lines (arcs), **ab** and **de**, and a half circle, **bd**. As indicated in the figure, the symbols L_l , L_c , L_r , L_m , d_l and d_r denote the lengths of the lines (arcs) **ab**, **bd**, **de**, **fc**, **af** and **fe**, respectively. Initial state (i): The tube is straight and its shape is symmetric with respect to the line **fc**, i.e., $d_l = d_r \equiv d_0$, $L_l = L_r = L_m \equiv L_0$ and thus $L_c = \pi d_0$. Intermediate state (ii): The tube curves with $d_l = d_r = d_0$ and $L_m = R\theta = L_0$. The point O is the center of bending curvature, R the radius of curvature of the arc **fc**, and θ the angle subtended by **fc**. The lengths $L_l = (R - d_0)\theta$, $L_r = (R + d_0)\theta$, and $L_c = \pi d_0$. Final state (iii): The spacing d_r decreases from d_0 with fixed R and θ . In state (iii), $d_l > d_0 > d_r$, $L_m = R\theta = L_0$, $L_l = (R - d_l)\theta$, $L_r = (R + d_r)\theta$, and $L_c = \pi(d_l + d_r)/2$. Because of area conservation (2), the width $(d_l + d_r)$ of state (iii) is greater than the initial value $2d_0$.

d_r and L_m . Consequently, the perimeter length L_{2D} (1) is also unchanged. In the final state (iii) the spacing d_r decreases from its original value d_0 while L_m is still unchanged. Equation (2) gives the change in the perimeter length L_{2D} from state (i) or (ii) to state (iii)

$$\delta L_{2D} = \frac{L_0 \Delta_d}{R} \left(-1 + \frac{\pi d_0 \hat{c}}{2L_0} \right) + \dots, \quad (3)$$

where $\Delta_d \equiv d_l - d_r$. It is obvious that $\delta L_{2D} < 0$ when $\Delta_d > 0$ and $d_0 \ll L_0$. In state (iii) Δ_d has to be greater than zero because of the area conservation (2). We now investigate how the tube's free energy changes with the parameters R and Δ_d .

3.2 Free Energy and Instability

The total free energy of the tube is given by

$$F_{2D} \equiv F_{2D}^b + F_{2D}^e, \quad (4)$$

where F_{2D}^b is the bending energy and F_{2D}^e the elastic energy associated with the tension in the perimeter. The interaction between the core and the perimeter is neglected for the sake of simplicity as well as clarity. We assume that the bending energy F_{2D}^b takes the form of

$$F_{2D}^b = \frac{\kappa_{2D}}{R^2} L_0 + a_0 \hat{c}, \quad (5)$$

where κ_{2D} is the bending stiffness of the tube, R the radius of bending curvature, and $L_0 = R\theta$ the tube length (Fig. 3). The last term $a_0 \hat{c}$ represents the contribution of the end cap **bd**. The tension Σ in the perimeter is defined as

$$\Sigma \equiv \frac{\partial F_{2D}^e}{\partial L_{2D}}, \quad (6)$$

where L_{2D} is the perimeter length (1). Now we can determine the difference in the total free energy F_{2D} between the initial state (i) and the final state (iii).

When the tube is deformed from state (i) to state (ii), only the bending energy F_{2D}^b (5) changes because d_l , d_r , L_m and thus L_{2D} are unchanged (Fig. 3). Therefore

$$F_{2D}^b[(ii)] - F_{2D}^b[(i)] = \frac{\kappa_{2D}}{R^2} L_0. \quad (7)$$

The change in F_{2D}^b from state (ii), where $\Delta_d = 0$, to state (iii), where $\Delta_d > 0$, is evidently given by

$$F_{2D}^b[(iii)] - F_{2D}^b[(ii)] = \frac{b_1(R)}{R} L_0 \Delta_d + b_2 \hat{c} + \mathcal{O}(\Delta_d^2). \quad (8)$$

The first two terms on the right-hand side of the above equation represent the lowest-order correction of the bending energy due to a change in Δ_d . The term $b_2 \hat{c}$, also a function of Δ_d , is the end cap contribution. Combining (7) and (8) leads to

$$\begin{aligned} \delta F_{2D}^b &\equiv F_{2D}^b[(iii)] - F_{2D}^b[(i)] \\ &= \frac{\kappa_{2D}}{R^2} L_0 + \frac{b_1(R)}{R} L_0 \Delta_d + b_2 \hat{c} + \mathcal{O}(\Delta_d^2) \\ &> 0. \end{aligned} \quad (9)$$

For cases with finite R , small Δ_d , and large aspect ratio ($L_0 \gg 2d_0$), equation (8) is much less than equation (7) and thus can be neglected. Equations (3) and (6) give the change in the elastic energy F_{2D}^e :

$$\begin{aligned} \delta F_{2D}^e &\equiv F_{2D}^e[(iii)] - F_{2D}^e[(i)] \\ &= \Sigma \cdot \delta L_{2D} + \frac{1}{2} \frac{\partial \Sigma}{\partial L_{2D}} (\delta L_{2D})^2 + \dots \\ &= \Sigma \frac{L_0 \Delta_d}{R} \left(-1 + \frac{\pi d_0 \hat{c}}{2L_0}\right) + \mathcal{O}(\Delta_d^2). \end{aligned} \quad (10)$$

Equations (9) and (10) lead to the change in F_{2D} (4) from state (i) to state (iii):

$$\begin{aligned} \delta F_{2D}(R, \Delta_d) &= \delta F_{2D}^b + \delta F_{2D}^e \\ &= \frac{L_0}{R} \left[\frac{\kappa_{2D}}{R} + \Delta_d (b_1 - \Sigma) \right] \\ &\quad + \hat{c} \left[b_2 + \frac{\pi d_0 \Sigma \Delta_d}{2R} \right] + \mathcal{O}(\Delta_d^2) \quad (11) \\ &\rightarrow \frac{L_0}{R} \left[\frac{\kappa_{2D}}{R} - \Delta_d \Sigma \right], \end{aligned}$$

where $b_1 \Delta_d$ is much less than κ_{2D}/R and thus neglected (see the text below (9)). Although $\delta F_{2D}^b \geq 0$, δF_{2D}^e and hence δF_{2D} can be negative. Consequently, if the perimeter tension Σ is large enough, a tube in state (i) would curve to lower its free energy. The equilibrium value of (R, Δ_d) can be determined if the $\mathcal{O}(\Delta_d^2)$ term in (11) is known. In addition, all the above equations involving the end cap show that as long as the tube is sufficiently long, the end cap contributions are negligible, i.e., \hat{c} can be set to zero.

3.3 Summary

We have shown that a two-dimensional tube of a given area is unstable against bending when the perimeter tension is sufficiently large. Owing to the area conservation, the perimeter length decreases when the tube undergoes the two-step deformation (Fig. 3). The decrease in the perimeter length reduces the elastic energy F_{2D}^e (6). Therefore, the tube can bend to lower its energy if the reduction in F_{2D}^e is larger than the increase in the bending energy F_{2D}^b . We also have shown that the end cap energy and its changes are negligible when the tube has a large aspect ratio, i.e., $L_0/2d_0 \gg 1$.

This two-dimensional case will serve as a paradigm for modeling myelin coiling in the following sections. In addition to the bilayer bending rigidity and the bilayer lateral tension, the inter-bilayer interaction will also be taken into consideration in our myelin model. We will employ the two-step deformation (Fig. 3) to determine the energy changes associated with myelin coiling.

4 Model Definition

The myelin model proposed in this section takes the bilayer tension and cylinder eccentricity into account (Sect.

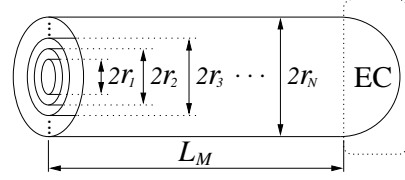


Figure 4: Model of an N -bilayer myelin. The myelin is composed of N nested bilayer cylinders. These cylinders may not be coaxial and moreover, they can bend cooperatively to yield myelin coiling (Figs. 5 and 6). The symbol r_n denotes the radius of the n -th cylinder, where $1 \leq n \leq N$. Since these bilayer cylinders need not be concentric, we label their diameters $2r_n$ instead of their radii r_n . The length L_n of the n -th bilayer cylinder is defined as that of its axis (Fig. 7), and the length L_M of a myelin as that of the innermost cylinder, i.e., $L_M \equiv L_1$. For a straight myelin, L_n and L_M are equal for all n , whereas for a curved myelin, they may not (Fig. 8). In this work we only consider myelins of large aspect ratios, i.e., $L_M/2r_N \gg 1$. Therefore the end caps (EC) of myelins can be neglected.

2). We postulate that the growth of myelins is sufficiently slow so that the myelins are in quasi-equilibrium and therefore their energies are well defined [16, 17]. In the following we will first specify the geometry and energy of a myelin and then describe how myelin coiling is modeled in this work. Like the two-dimensional case of the previous section, the proposed coiling mechanism is analogous to the Euler buckling of an elastic rod subject to axial compression [20].

4.1 Myelin Geometry

An N -bilayer myelin is a multilamellar tube composed of a nested stack of N cylindrical fluid bilayers (Fig. 4). These bilayer cylinders need not be coaxial (Fig. 5) and may curve collectively to give rise to myelin coiling (Fig. 6). In addition, we only consider myelins of large aspect ratios so that the end caps are negligible. The symbol r_n denotes the radius of the n -th bilayer cylinder, with $n = 1$ and $n = N$ corresponding to the innermost and outermost cylinders, respectively (Fig. 4). We define the length L_n of the n -th bilayer cylinder as that of its axis and the length L_M of a myelin as that of the innermost cylinder, i.e., $L_M \equiv L_1$ (Figs. 4 and 7). With this myelin model we can now describe the geometry of a coiled myelin.

A coiled myelin is composed of nested helical bilayer cylinders (Fig. 6). The following parametric expression for a helix describes the axis of the n -th bilayer cylinder:

$$\mathbf{R}_n(\phi) = (\rho_n \cos \phi, \rho_n \sin \phi, P\phi/2\pi), \quad (12)$$

where ϕ , ρ_n and P are defined in Figure 6. The radius of

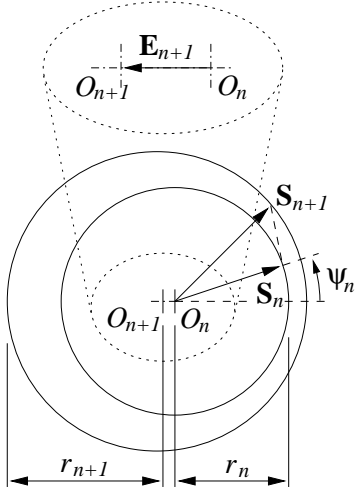


Figure 5: Cross-sectional view of two adjacent bilayer cylinders in a myelin. We describe the n -th and $(n+1)$ -th cylinders with the vectors \mathbf{S}_n and \mathbf{S}_{n+1} , and their axes with O_n and O_{n+1} , respectively. When two nested cylinders are not concentric, the spacing between them is clearly not uniform (Fig. 8). In this work we define the spacing d_n between the n -th and $(n+1)$ -th cylinders as $d_n(\mathbf{S}_n) = \min\{|\mathbf{S}_{n+1} - \mathbf{S}_n|\}$. To calculate $d_n(\mathbf{S}_n)$, we select the coordinate system with O_n being the coordinate origin and $\mathbf{S}_n = (r_n \cos \psi_n, r_n \sin \psi_n)$. The eccentricity vector $\mathbf{E}_{n+1} \equiv (\delta_{n+1}, 0)$ represents the positional difference between O_{n+1} and O_n , as shown in the oval inset. Given δ_{n+1} , the inter-bilayer spacing $d_n(\mathbf{S}_n) = r_{n+1} - (r_n^2 + \delta_{n+1}^2 - 2r_n\delta_{n+1} \cos \psi_n)^{1/2}$. For convenience we set $\delta_1 \equiv 0$.

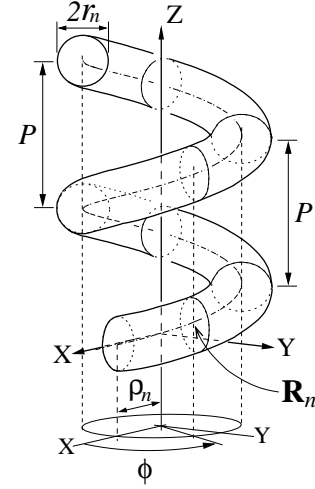


Figure 6: Coiling of a myelin. For clarity we only show the n -th bilayer cylinder (Fig. 4). The axis of this coiled cylinder forms a helix described by the parametric equation $\mathbf{R}_n(\phi) = (\rho_n \cos \phi, \rho_n \sin \phi, P\phi/2\pi)$, where ρ_n is the radius of the circular projection of the helix on the X-Y plane and P the pitch of the helix.

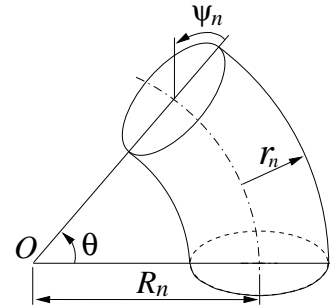


Figure 7: Bending of the n -th bilayer cylinder. The point O is the center of bending curvature. The cylinder length $L_n \equiv R_n\theta$, where R_n is the radius of bending curvature (13) and θ the angle subtended by the cylinder. This cylinder can be viewed as a section of a torus of radii r_n and R_n . Straight cylinders correspond to cases with $R_n \rightarrow \infty$, $\theta \rightarrow 0$, and finite $R_n\theta$. The surface area element $dA_n = r_n d\psi_n (R_n + r_n \cos \psi_n) d\theta$. The two principal curvatures of the surface are $1/r_n$ and $\cos \psi_n / (R_n + r_n \cos \psi_n)$.

curvature of the helix \mathbf{R}_n is equal to

$$R_n = \rho_n \left(1 + \frac{P^2}{4\pi^2 \rho_n^2} \right). \quad (13)$$

The volume V_n , area A_n and length L_n of the n -th bilayer cylinder are given by

$$V_n = \pi r_n^2 L_n, \quad (14)$$

$$A_n = 2\pi r_n L_n, \quad (15)$$

$$L_n = 2\pi \rho_n \left[1 + \frac{P^2}{4\pi^2 \rho_n^2} \right]^{1/2} t_c, \quad (16)$$

where r_n is the radius of the cylinder and t_c the number of turns of the coiling (Fig. 6). Strictly speaking, A_n is the projected area of the n -th bilayer [19]. The true bilayer area is larger than A_n because of thermal undulations of the bilayer.

4.2 Free Energy

The total energy F of a myelin includes the curvature energy F^c of bilayers, the elastic energy F^e associated with bilayer lateral tension, and the inter-bilayer interaction energy F^i :

$$F \equiv F^c + F^e + F^i. \quad (17)$$

The curvature energy E^c of a membrane of area A takes the form of

$$E^c = \frac{\kappa}{2} \int_A dA (K_1 + K_2 - K_0)^2, \quad (18)$$

where κ is the bending stiffness, and K_1 and K_2 are the principal curvatures [23]. The spontaneous curvature K_0 is taken to be zero for simplicity. (See the Discussion section.) The Gaussian curvature term ($\sim \int dA K_1 K_2$) is neglected because the myelin coiling investigated here does not involve any topological changes. Thus, there can be no change in this energy according to the Gauss-Bonnet theorem [24]. Because of the fluid nature of bilayers, a myelin can not sustain torsional stress in its axial direction. Therefore the curvature energy change of a myelin due to coiling depends only on the bending of its constituent cylinders (Figs. 6 and 7). Using (13) and (18), with the area element $dA_n = r_n d\psi_n (R_n + r_n \cos \psi_n) d\theta$ and the two principal curvatures $1/r_n$ and $\cos \psi_n / (R_n + r_n \cos \psi_n)$ (Fig. 7), the curvature energy E_n^c of the n -th bilayer cylinder in a coiled myelin is given by

$$\begin{aligned} E_n^c &= \frac{\pi \kappa L_n}{r_n \sqrt{1 - (r_n/R_n)^2}} \\ &= \frac{\pi \kappa L_n}{r_n} + \frac{\pi \kappa r_n L_n}{2R_n^2} \left[1 + \frac{3}{4} \frac{r_n^2}{R_n^2} + \dots \right], \end{aligned} \quad (19)$$

where $L_n = R_n \theta$ is the cylinder length. The above equation suggests that the curvature energy of a curved bilayer cylinder can be written as a sum of the energy

($\sim 1/r_n$) associated with local bending of the bilayer and that ($\sim 1/R_n^2$) resulting from bending of the cylinder (13). Equation (19) leads to the curvature energy F^c of a coiled N -bilayer myelin:

$$\begin{aligned} F^c &= \sum_{n=1}^N E_n^c \\ &= \sum_{n=1}^N \frac{\pi \kappa L_n}{r_n} + \sum_{n=1}^N \frac{\tilde{\kappa}_n L_n}{2R_n^2}, \end{aligned} \quad (20)$$

where the bending modulus $\tilde{\kappa}_n$ of the n -th bilayer cylinder is defined as

$$\tilde{\kappa}_n \equiv \pi \kappa r_n \left[1 + \frac{3}{4} \frac{r_n^2}{R_n^2} + \dots \right]. \quad (21)$$

The lateral tension of a bilayer arises from stretching the bilayer area from the relaxed state [19, 25, 26]. For a fluid bilayer, the tension is uniform and isotropic. Let F_n^e denote the elastic energy giving rise to the tension σ_n in the n -th bilayer cylinder, i.e.,

$$\sigma_n \equiv \frac{\partial F_n^e}{\partial A_n}, \quad (22)$$

where A_n is the area of the cylinder (15). The elastic energy F^e of an N -bilayer myelin is then given by

$$F^e = \sum_{n=1}^N F_n^e. \quad (23)$$

The energy F^i describes the net result of all kinds of inter-bilayer interactions such as van der Waals attraction, electrostatic repulsion [2], hydration pressure [27], and the Helfrich repulsion [28]. For an N -bilayer myelin, F^i can be conveniently expressed as

$$F^i = \sum_{n=1}^{N-1} F_n^i, \quad (24)$$

where F_n^i represents the energy of interaction between the n -th and $(n+1)$ -th bilayers. We expect that F_n^i can be written as

$$F_n^i \equiv \int_{A_n} dA_n f_n^i(d_n(\mathbf{S}_n), \sigma_n, \sigma_{n+1}), \quad (25)$$

where f_n^i denotes the interaction energy F_n^i per unit area of the n -th bilayer and $d_n(\mathbf{S}_n)$, defined in Figure 5, is the spacing between the n -th and $(n+1)$ -th bilayers. For simplicity we assume that f_n^i depends only on the spacing d_n and the tensions σ_n and σ_{n+1} (22). This implies $f_n^i(d_n, \sigma_n, \sigma_{n+1}) = f_n^i(d_n, \sigma_{n+1}, \sigma_n)$ since the effect of the bilayer curvatures is neglected [16]. Because the bilayer cylinders may not be coaxial, we define the inter-bilayer spacing $d_n(\mathbf{S}_n)$ as the shortest distance from the point \mathbf{S}_n

on the n -th cylinder to the $(n+1)$ -th cylinder: With δ_{n+1} and ψ_n defined in Figure 5,

$$\begin{aligned}
d_n(\mathbf{S}_n) &\equiv d_n(\psi_n, \delta_{n+1}) \\
&= r_{n+1} - (r_n^2 + \delta_{n+1}^2 - 2r_n\delta_{n+1}\cos\psi_n)^{1/2} \\
&= (r_{n+1} - r_n) + \delta_{n+1} \left[\cos\psi_n - \frac{\sin^2\psi_n}{2} \frac{\delta_{n+1}}{r_n} \right. \\
&\quad \left. - \frac{\cos\psi_n \sin^2\psi_n}{2} \frac{\delta_{n+1}^2}{r_n^2} + \mathcal{O}\left(\frac{\delta_{n+1}^3}{r_n^3}\right) \right]. \quad (26)
\end{aligned}$$

The potential f_n^i gives rise to an inter-bilayer pressure

$$p_n \equiv -\frac{\partial f_n^i}{\partial d_n}. \quad (27)$$

This pressure may not be equal to the real inter-bilayer pressure \mathcal{P}_n owing to the fact that the definitions of f_n^i and d_n are artificial. Nonetheless, p_n should be a good approximation to \mathcal{P}_n , especially when $|\delta_{n+1}| \ll (r_{n+1} - r_n)$. For typical myelins, we expect $p_n > 0$ [16] and moreover, p_n should satisfy the force balance equation for the n -th bilayer (Laplace's formula) [29]:

$$\sigma_n \approx \frac{dp_n^w + p_{n-1} - p_n}{K_{n1} + K_{n2}}, \quad (28)$$

where dp_n^w is the water pressure difference across the bilayer, and K_{n1} and K_{n2} are the two principal curvatures of the bilayer (see (18) and Fig. 7).

4.3 Modeling Myelin Coiling

The myelin structure defined in this work has three important properties: (a) it is postulated to be in quasi-equilibrium owing to its slow growth rate (Sect. 2) [16, 17], (b) the bilayer tension may vary from bilayer to bilayer, and (c) the constituent bilayer cylinders can be non-coaxial. Given these properties, we will demonstrate that coiling may lead to a decrease in the elastic energy F^e (23). Therefore, a straight myelin is unstable to coiling if the decrease in F^e is large enough to compensate for the net increase in other energies (see (17), (20), and (24)). In Section 5 we will derive the energy changes associated with myelin coiling. By analyzing a two-bilayer case in detail in Section 6, we will show that coiling may indeed lower the myelin energy.

We will employ the two-step deformation developed in Section 3 to investigate the energy changes due to myelin coiling (Figs. 3 and 8). For the sake of simplicity, two constraints are imposed. First, the myelin length L_M is fixed during the deformation (Fig. 4). As in the two-dimensional case (cf. the text below (1)), this artificial constraint would not invalidate our model. Secondly, we do not allow exchange of material, surfactant or water, between bilayers. Because water and bilayers are virtually incompressible under moderate pressure [27], this constraint implies that the

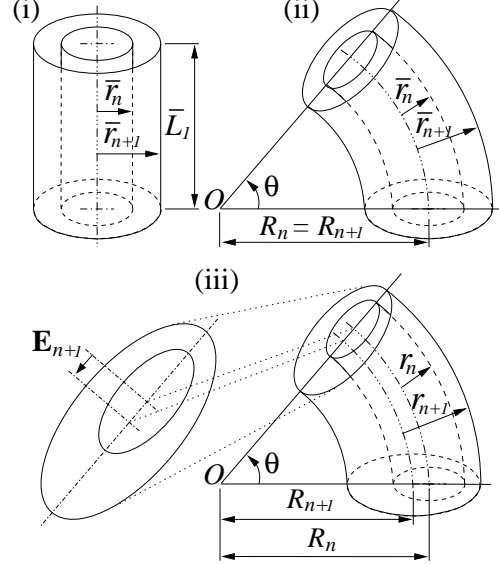


Figure 8: Two-step deformation of a myelin. As in Figure 3, this procedure transforms a myelin from state (i) into state (ii) and then into state (iii), with the constraints of fixed myelin length and fixed volume for each bilayer cylinder. For clarity we only show two adjacent bilayer cylinders (Fig. 5). Initial state (i): The myelin consists of straight, coaxial bilayer cylinders with radii $r_n = \bar{r}_n$ and myelin length $L_M \equiv L_1 = \bar{L}_1 = \bar{L}_n$ (Fig. 4). Intermediate state (ii): The myelin curves while its constituent cylinders are still coaxial. In this state $R_n = R_1$. The constraints yield that $R_n\theta = \bar{L}_1$, $r_n = \bar{r}_n$, and therefore $A_n = \bar{A}_n$ (see (14) and (15)). Final state (iii): The cylinders are no longer coaxial. The eccentricity vector \mathbf{E}_{n+1} is defined in Figure 5. All the cylinders except for the innermost one ($n = 1$) may move toward the center O of bending curvature, i.e., $\delta_{n+1} \leq 0$. In state (iii), $r_1 = \bar{r}_1$, $L_1 = \bar{L}_1$, $R_{n+1} = R_n + \delta_{n+1} \leq R_n$, and therefore $L_{n+1} = R_{n+1}\theta \leq L_n = R_n\theta$. The constraints lead to $r_n \geq \bar{r}_n$ and $A_n \leq \bar{A}_n$ for $n > 1$ (see (30) and (31)).

volume of each bilayer cylinder is conserved during the deformation. (See the Discussion section.)

Figure 8 gives a detailed description of the two-step deformation. The myelin is deformed from state (i) into state (ii) and then into state (iii). In state (i) the myelin is straight and its constituent bilayer cylinders are concentric, i.e., $\mathbf{E}_n = \mathbf{0}$ for all n . From (i) to (ii), the myelin curves with the condition that the bilayer cylinders are still concentric. As a result, the curvature energy F^c increases while the elastic energy F^e and the inter-bilayer interaction F^i remain unchanged. From (ii) to (iii), the cylinders are displaced so that they are no longer coaxial (Fig. 5). In this step the displacement δ_n may become negative for $n > 1$, reducing the bilayer area A_n and thus the elastic energy F^e .

Hereinafter, symbols like \bar{r}_n , \bar{L}_n , and \bar{p}_n with an over-head bar refer to the initial state (i), where the myelin is straight, and those without refer to the final state (iii), where the myelin is curved (Fig. 8). The terms ‘‘coiling’’ and ‘‘bending’’ are used interchangeably because they are energetically equivalent for myelins composed of fluid bilayers. Since the myelins considered here have large aspect ratios, their end caps are neglected. However, the end caps can be neglected only in terms of energy calculation. Their presence is necessary for volume conservation and force cancellation (cf. text below (1)).

5 Bending of a Myelin

Now we will use the model defined in the previous section to investigate myelin coiling. As in Section 3, we will first derive the geometrical changes of a myelin undergoing the two-step deformation (Fig. 8). Then we will determine the respective energy changes. For a myelin composed of N bilayers, state (iii) is described by N parameters, $R_1, \delta_2, \dots, \delta_{N-1}$, and δ_N ($\delta_1 \equiv 0$; see Fig. 5).

The two-step deformation is constrained by the conditions of fixed myelin length $L_M \equiv L_1 = \bar{L}_1 = \bar{L}_n$ and volume conservation $V_n = \bar{V}_n$ for each bilayer cylinder (Sect. 4.3). With these two constraints and (Figs. 4, 5, and 8)

$$R_n = R_1 + \sum_{j=1}^n \delta_j,$$

the length L_n , radius r_n , and area A_n of the n -th bilayer cylinder in state (iii) are given by ((14) and (15))

$$L_n \equiv R_n \theta = \bar{L}_n \left(1 + \sum_{j=1}^n \frac{\delta_j}{R_1} \right) \leq \bar{L}_n, \quad (29)$$

$$r_n = \bar{r}_n \left(1 + \sum_{j=1}^n \frac{\delta_j}{R_1} \right)^{-1/2} \geq \bar{r}_n, \quad (30)$$

$$A_n = \bar{A}_n \left(1 + \sum_{j=1}^n \frac{\delta_j}{R_1} \right)^{1/2} \leq \bar{A}_n, \quad (31)$$

where $\delta_1 = 0$ by construction and $\delta_n \leq 0$ for $n > 1$. Equation (30) implies that not only $r_{n+1} \geq \bar{r}_{n+1}$ but also $(r_{n+1} - r_n) \geq (\bar{r}_{n+1} - \bar{r}_n)$, i.e., both r_{n+1} and $(r_{n+1} - r_n)$ increase when the myelin is transformed from state (i) to state (iii). The increase in $(r_{n+1} - r_n)$ hints the possibility of a decrease in the inter-bilayer interaction F_n^i (25). Merging (26) and (30) leads to the change in the inter-bilayer spacing

$$\begin{aligned} \delta d_n &\equiv d_n[(\text{iii})] - d_n[(\text{i})] \\ &= d_n(\mathbf{S}_n) - (\bar{r}_{n+1} - \bar{r}_n) \\ &= \delta d_{n1} + \delta d_{n2}, \end{aligned} \quad (32)$$

where

$$\begin{aligned} \delta d_{n1} &= -\frac{\bar{r}_{n+1} \delta_{n+1}}{2 R_1} - \frac{(\bar{r}_{n+1} - \bar{r}_n)}{2} \sum_{j=1}^n \frac{\delta_j}{R_1} \\ &+ \frac{3\bar{r}_{n+1}}{8} \left(\sum_{j=1}^{n+1} \frac{\delta_j}{R_1} \right)^2 - \frac{3\bar{r}_n}{8} \left(\sum_{j=1}^n \frac{\delta_j}{R_1} \right)^2 \\ &+ \mathcal{O} \left(\frac{\delta_i \delta_j \delta_k}{R_1^3} \right) \end{aligned}$$

and

$$\begin{aligned} \delta d_{n2} &= \delta_{n+1} \left[\cos \psi_n - \frac{\sin^2 \psi_n \delta_{n+1}}{2 \bar{r}_n} \right. \\ &\quad \left. - \frac{\cos \psi_n \sin^2 \psi_n \delta_{n+1}^2}{2 \bar{r}_n^2} + \dots \right]. \end{aligned}$$

Equation (31) gives rise to the area change

$$\begin{aligned} \delta A_n &\equiv A_n[(\text{iii})] - A_n[(\text{i})] \\ &= \frac{\bar{A}_n}{2} \sum_{j=1}^n \frac{\delta_j}{R_1} - \frac{\bar{A}_n}{8} \left(\sum_{j=1}^n \frac{\delta_j}{R_1} \right)^2 \\ &+ \mathcal{O} \left(\frac{\delta_i \delta_j \delta_k}{R_1^3} \right) \leq 0, \end{aligned} \quad (33)$$

where $\delta_1 = 0$ and thus $\delta A_1 = 0$. Equations (29)–(33) allow us to calculate the energy changes due to the two-step deformation, as shown below.

The curvature energy change (cf. (20))

$$\begin{aligned} \delta F^c &\equiv F^c[(\text{iii})] - F^c[(\text{i})] \\ &= \sum_{n=1}^N \frac{\bar{A}_n}{2} \left[\frac{\bar{\kappa}_n}{2\pi \bar{r}_n R_1^2} + g_n \sum_{j=1}^n \frac{\delta_j}{R_1} \right] \\ &+ \mathcal{O} \left(\frac{\delta_i \delta_j}{R_1^2} \right) > 0, \end{aligned} \quad (34)$$

where $\bar{L}_n = \bar{A}_n/2\pi\bar{r}_n = \bar{L}_1$ and (cf. (21))

$$\bar{\kappa}_n \equiv (\bar{\kappa}_n)_i = \pi\kappa\bar{r}_n \left[1 + \frac{3}{4} \frac{\bar{r}_n^2}{R_1^2} + \dots \right]. \quad (35)$$

The first-order terms ($\sim g_n \sum \delta_j$) in (34) result from the second step of the deformation. The exact functional form of g_n is unimportant because the lowest-order terms ($\sim \bar{\kappa}_n$) dominate. This is also intuitively reasonable in that when $\sum \delta_n \ll R_1 < \infty$, the major contribution to δF^c should come from the deformation from (i) to (ii) (Fig. 8). Therefore we will not derive g_n here.

Equation 33 shows that for $n > 1$, the area A_n decreases in the two-step deformation. This in turn reduces the elastic energy F^e (see (22) and (23)). With (33) the change in F^e is given by

$$\begin{aligned} \delta F^e &\equiv F^e[(iii)] - F^e[(i)] = \sum_{n=1}^N \delta F_n^e \\ &= \sum_{n=1}^N \left[\left(\frac{\partial F_n^e}{\partial A_n} \right)_i \delta A_n + \frac{1}{2} \left(\frac{\partial^2 F_n^e}{\partial A_n^2} \right)_i \delta A_n^2 + \dots \right] \\ &= \sum_{n=1}^N \frac{\bar{A}_n \bar{\sigma}_n}{2} \sum_{j=1}^n \frac{\delta_j}{R_1} \\ &\quad + \sum_{n=1}^N \frac{\bar{A}_n}{8} \left[\left(\frac{\partial \sigma_n}{\partial A_n} \right)_i \bar{A}_n - \bar{\sigma}_n \right] \left(\sum_{j=1}^n \frac{\delta_j}{R_1} \right)^2 \\ &\quad + \mathcal{O} \left(\frac{\delta_i \delta_j \delta_k}{R_1^3} \right), \end{aligned} \quad (36)$$

where $\delta F_1^e = 0$ since $\delta A_1 = 0$.

The change in the inter-bilayer interaction F^i (24) takes a complex form because $\delta A_n \neq 0$ and $\delta \sigma_n \neq 0$ for $n > 1$:

$$\begin{aligned} \delta F^i &\equiv F^i[(iii)] - F^i[(i)] = \sum_{n=1}^{N-1} \delta F_n^i \\ &= \sum_{n=1}^{N-1} \delta \int_{A_n} dA_n f_n^i(d_n(\mathbf{S}_n), \sigma_n, \sigma_{n+1}), \end{aligned}$$

where f_n^i is defined in (25). Expanding the above equation around state (i) results in

$$\begin{aligned} \delta F^i &= \sum_{n=1}^{N-1} \int_{\bar{A}_n} d\bar{A}_n \left[-\bar{p}_n \delta d_n - \left(\frac{\partial p_n}{\partial d_n} \right)_i \frac{\delta d_n^2}{2} \right. \\ &\quad \left. + \left(\frac{\partial f_n^i}{\partial \sigma_n} \right)_i \delta \sigma_n + \left(\frac{\partial f_n^i}{\partial \sigma_{n+1}} \right)_i \delta \sigma_{n+1} \right] \\ &\quad + \sum_{n=1}^{N-1} \delta A_n \bar{f}_n^i + \dots, \end{aligned} \quad (37)$$

where the area element (Fig. 7)

$$d\bar{A}_n = R_1 d\theta \cdot \bar{r}_n d\psi_n \left(1 + \frac{\bar{r}_n}{R_1} \cos \psi_n \right),$$

the inter-bilayer pressure of state (i) (cf. (27))

$$\bar{p}_n = - \left(\frac{\partial f_n^i}{\partial d_n} \right)_i, \quad (38)$$

and the spacing change δd_n is given by (32). Using (33) and

$$\delta \sigma_n = \left(\frac{\partial \sigma_n}{\partial A_n} \right)_i \delta A_n + \left(\frac{\partial^2 \sigma_n}{\partial A_n^2} \right)_i \frac{\delta A_n^2}{2} + \dots, \quad (39)$$

we determine the change in the inter-bilayer interaction energy as well as the net change in the myelin energy ((17), (34), and (36)):

$$\begin{aligned} \delta F^i &= \sum_{n=1}^{N-1} \frac{\bar{A}_n}{2} \left[\sum_{k=2}^3 C_{nk} \sum_{j=1}^{n+1} \frac{\delta_j}{R_1} + C_{n4} \sum_{j=1}^n \frac{\delta_j}{R_1} \right. \\ &\quad \left. + C_{n5} \delta_{n+1}^2 \right] + \mathcal{O} \left(\frac{\delta_i \delta_j}{R_1^2}, \delta_{n+1}^4 \right) \end{aligned} \quad (40)$$

and

$$\begin{aligned} \delta F &\equiv F[(iii)] - F[(i)] = \delta F^c + \delta F^e + \delta F^i \\ &= \sum_{n=1}^N \frac{\bar{A}_n}{2} \left[\mathcal{B}_n + \sum_{k=0}^1 C_{nk} \sum_{j=1}^n \frac{\delta_j}{R_1} \right] \\ &\quad + \sum_{n=1}^{N-1} \frac{\bar{A}_n}{2} \left[\sum_{k=2}^3 C_{nk} \sum_{j=1}^{n+1} \frac{\delta_j}{R_1} + C_{n4} \sum_{j=1}^n \frac{\delta_j}{R_1} \right. \\ &\quad \left. + C_{n5} \delta_{n+1}^2 \right] + \mathcal{O} \left(\frac{\delta_i \delta_j}{R_1^2}, \delta_{n+1}^4 \right) \end{aligned} \quad (41)$$

where

$$\mathcal{B}_n = \frac{\bar{\kappa}_n}{2\pi\bar{r}_n R_1^2} \approx \frac{\kappa}{2R_1^2} > 0, \quad (42)$$

$$C_{n0} = g_n,$$

$$C_{n1} = \bar{\sigma}_n,$$

$$C_{n2} = (\bar{r}_{n+1} - \bar{r}_n) \bar{p}_n,$$

$$C_{n3} = \left(\frac{\partial f_n^i}{\partial \sigma_{n+1}} \right)_i \left(\frac{\partial \sigma_{n+1}}{\partial A_{n+1}} \right)_i \bar{A}_{n+1},$$

$$\begin{aligned} C_{n4} &= \left(\frac{\partial f_n^i}{\partial \sigma_n} \right)_i \left(\frac{\partial \sigma_n}{\partial A_n} \right)_i \bar{A}_n + \bar{f}_n^i \\ &= \left[\frac{\partial (f_n^i A_n)}{\partial A_n} \right]_i = \left(\frac{\partial F_n^i}{\partial A_n} \right)_i, \end{aligned} \quad (43)$$

$$C_{n5} = -\frac{1}{2} \left(\frac{\partial p_n}{\partial d_n} \right)_i, \quad (44)$$

$\delta_1 = 0$ by definition, and $\delta_n \leq 0$ for $n > 1$. In spite of the fact that equation (41) allows δ_n to be positive or negative, we are only interested in the cases where $\delta_n \leq 0$ (Figs. 5 and 8). The terms \mathcal{B}_n and C_{n0} come from the curvature energy F^c (20), C_{n1} from the elastic energy F^e (23), and

$\mathcal{C}_{n2} - \mathcal{C}_{n5}$ from the inter-bilayer interaction energy F^i (24). As mentioned in the text below (35), \mathcal{C}_{n0} is negligible. In addition, we expect $p_n > 0$ and $(\partial p_n / \partial d_n) < 0$ for myelins [16]. Equation (41) seems too complicated to be useful for investigating myelin coiling: there are $2N$ initial conditions, $\bar{\sigma}_n$ and \bar{r}_n , and N independent parameters, R_1 and δ_n ($\delta_1 \equiv 0$; see Fig. 5). However, this equation is not as worthless as it seems. In order for a myelin to coil, δF (41) has to be less than zero. The two-dimensional case of Section 3 suggests that if some of the bilayer tensions $\bar{\sigma}_n$ are sufficiently large, the decrease in F^e (36) might be large enough to yield a negative δF . In the next section we will show that the proposed mechanism of myelin coiling can be easily understood with the special case of $N = 2$. The enormous number of parameters in equation (41) merely reflects the complexity of myelinic structures: for instance, two apparently similar myelins may have very different bilayer tension profiles and therefore one may coil and the other may not.

6 Bending of a Two-bilayer Myelin

In this section we inspect closely a special case of myelin coiling, where the myelin is composed of only two bilayers, i.e., $N = 2$. One may think of this two-bilayer myelin as a generalization of the two-dimensional tube of Section 3. Besides, equation (41) suggests that in terms of energy calculation, an N -bilayer myelin can be viewed as a multilamellar tube composed of $(N - 1)$ nested two-bilayer myelins. Therefore the results of this two-bilayer case should be applicable to multiple-bilayer myelins. In the following we will first derive a simple criterion of coiling instability for a two-bilayer myelin and study a numerical example in detail in Sections 6.1 and 6.2. Then in Section 6.3 we will show how this two-bilayer example can be generalized for myelins of many bilayers

For a two-bilayer myelin, two independent parameters R_1 and δ_2 determine state (iii) (Figs. 5 and 8). Equation (41) can be rewritten as

$$\begin{aligned} \delta F &\equiv F[(\text{iii})] - F[(\text{i})] \\ &= \frac{\bar{A}_1}{2} \left[\mathcal{B} + \frac{\delta_2}{R_1} \sum_{k=0}^3 \mathcal{C}_k + \mathcal{C}_5 \delta_2^2 \right] \\ &\quad + \mathcal{O} \left(\frac{\delta_2^2}{R_1^2}, \delta_2^4 \right), \end{aligned} \quad (45)$$

where $\delta_2 \leq 0$ (Figs. 5 and 8),

$$\begin{aligned} \mathcal{B} &= \mathcal{B}_1 + \mathcal{B}_2 \frac{\bar{A}_2}{\bar{A}_1} = \frac{\bar{\kappa}_1 + \bar{\kappa}_2}{2\pi\bar{r}_1 R_1^2} > 0, \\ \mathcal{C}_0 &= \mathcal{C}_{20} \frac{\bar{A}_2}{\bar{A}_1} = g_2 \frac{\bar{r}_2}{\bar{r}_1}, \end{aligned}$$

$$\mathcal{C}_1 = \mathcal{C}_{21} \frac{\bar{A}_2}{\bar{A}_1} = \bar{\sigma}_2 \frac{\bar{r}_2}{\bar{r}_1} > 0, \quad (46)$$

$$\mathcal{C}_2 = \mathcal{C}_{12} = (\bar{r}_2 - \bar{r}_1) \bar{p}_1 > 0, \quad (47)$$

$$\mathcal{C}_3 = \mathcal{C}_{13} = \left(\frac{\partial f_1^i}{\partial \sigma_2} \right)_i \left(\frac{\partial \sigma_2}{\partial \bar{A}_2} \right)_i \bar{A}_2 < 0, \quad (48)$$

$$\mathcal{C}_5 = \mathcal{C}_{15} = -\frac{1}{2} \left(\frac{\partial p_1}{\partial d_1} \right)_i > 0, \quad (49)$$

and \mathcal{C}_{14} (43) does not exist because $\delta A_1 = 0$ (33) and $\delta \sigma_1 = 0$ ((37) and (39)). Although equation (45) does not dictate the sign of δ_2 , we only consider the case of $\delta_2 \leq 0$ because of the two-step deformation (Figs. 5 and 8). The terms \mathcal{B} and \mathcal{C}_0 originate from the curvature energy F^c (20), \mathcal{C}_1 from the elastic energy F^e (23), and \mathcal{C}_2 , \mathcal{C}_3 , and \mathcal{C}_5 from the inter-bilayer interaction energy F^i (24). Here we assume that the outer bilayer is under tension ($\bar{\sigma}_2 > 0$) and the inter-bilayer interaction is repulsive ($\bar{p}_1 > 0$). We expect $\mathcal{C}_3 < 0$ and $\mathcal{C}_5 > 0$ because the inter-bilayer repulsion increases as the bilayer tension σ_2 or the inter-bilayer spacing d_1 decreases, i.e., $\partial f_1^i / \partial \sigma_2 < 0$ and $(\partial p_1 / \partial d_1) < 0$. Therefore, \mathcal{C}_1 and \mathcal{C}_2 contribute to coiling, while \mathcal{C}_3 and \mathcal{C}_5 hinder coiling.

6.1 Criterion of Coiling Instability

Equation (45) gives rise to a simple stability criterion when all the $\mathcal{O}(\delta_2^2)$ terms are negligible: a straight, two-bilayer myelin is unstable against bending or coiling if there exists a set of (δ_2, R_1) such that

$$\delta F \sim \mathcal{B} + \frac{\delta_2}{R_1} [\mathcal{C}_1 + \mathcal{C}_2 + \mathcal{C}_3] < 0, \quad (50)$$

where \mathcal{C}_0 is dropped because $\mathcal{B} \gg |\mathcal{C}_0 \delta_2 / R_1|$ (see the text below (35)). By setting $\delta F = 0$ we can define a threshold of δ_2 , denoted as δ_{th} , for coiling instability. If one can find a finite R_1 and a negative δ_2 of magnitude larger than $|\delta_{\text{th}}|$, then state (iii) is energetically more favorable than state (i) (Fig. 8). However, δ_2 and R_1 must be bounded by the geometry of the myelin: for example, $|\delta_2|$ must be less than $(\bar{r}_2 - \bar{r}_1)$, and R_1 must be greater than r_2 . The equilibrium value of (δ_2, R_1) can be determined when the terms of $\mathcal{O}(\delta_2^2)$ in (45) are known.

If the tension $\bar{\sigma}_2$ is large enough so that $\mathcal{C}_1 \gg |\mathcal{C}_2 + \mathcal{C}_3|$, i.e., the inter-bilayer interaction is negligible, criterion (50) is reduced to

$$\delta F \sim \mathcal{B} + \frac{\delta_2}{R_1} \mathcal{C}_1 < 0. \quad (51)$$

Furthermore, when $\bar{r}_2 \approx \bar{r}_1 \gg (\bar{r}_2 - \bar{r}_1)$, we expect $\mathcal{B} \approx \kappa / R_1^2$ (see (35) and (42)) and $\mathcal{C}_1 \approx \bar{\sigma}_2$. In such case the δ_2 threshold for coiling is given by

$$\delta_{\text{th}} = -\frac{\kappa}{\bar{\sigma}_2 R_1}. \quad (52)$$

Now we investigate a two-bilayer myelin composed of typical lipid bilayers with parameters

$$\bar{r}_2 = 20 \mu\text{m} \text{ (Fig. 1),}$$

$$\begin{aligned}
\bar{d}_1 &= \bar{r}_2 - \bar{r}_1 = 2.4 \text{ nm} [27], \\
R_1 &= 30 \text{ } \mu\text{m} [8, 11, 13], \\
\kappa &= 10^{-12} \text{ erg} [19], \\
dp_2^w &= 0 \text{ dyne/cm}^2 \text{ (Eq. (28))}, \\
\bar{p}_1 &= 10^3 \text{ dyne/cm}^2 \text{ (Eq. (38))} [9, 16],
\end{aligned}$$

and the temperature $T = 4.1 \times 10^{-14}$ erg (300 K). For simplicity the water pressure difference dp_2^w is assumed to be zero. The values of these parameters are carefully chosen such that the results of this example can be readily generalized for myelins of many bilayers (Sect. 6.3). Equation (28) with the above parameters implies $\mathcal{C}_1 \approx \bar{\sigma}_2 \approx \bar{r}_2 \bar{p}_1 = 2$ dyne/cm [25, 26] and thus $\delta_{\text{th}} \approx -0.02 \text{ \AA}$ according to (52). Because $|\delta_{\text{th}}|$ is much less than typical bilayer thickness or inter-bilayer spacing (Fig. 1) [27], there exists a negative δ_2 such that $|\delta_2| > |\delta_{\text{th}}|$. Therefore state (iii) is more stable than state (i) (see (50) and Fig. 8). This numerical example suggests that criterion (51) can be met easily and a two-bilayer myelin may bend or coil if the lateral tension of the outer bilayer is sufficiently large. However, two questions arise with regard to the above example. Can we ignore the $\mathcal{O}(\delta_2^2)$ terms in equation (45)? Moreover, is the inter-bilayer interaction negligible, i.e., is it possible that $\mathcal{C}_1 \gg |\mathcal{C}_2 + \mathcal{C}_3|$? Because the complete functional form of f_n^i (25) is not known, it seems difficult, if not impossible, to answer these two questions with logical rigor. In the next subsection we will try to address these issues by means of some physical arguments.

In fact, equation (52) can also be viewed from another perspective: it provides a lower bound for $\bar{\sigma}_2$ in a coiled myelin when $|\delta_{\text{th}}|$ is replaced with the inter-bilayer spacing, i.e., a coiled two-bilayer myelin with coiling curvature $1/R_1$ (13) must have a $\bar{\sigma}_2$ greater than $\kappa/(\bar{d}_1 R_1)$. The actual $\bar{\sigma}_2$ is expected to be larger than this value because of the contributions from the inter-bilayer interaction, the higher-order terms in E_n^c (19), and the $\mathcal{O}(\delta_2^2)$ terms in (45). In principle, we can obtain a more sophisticated lower bound for $\bar{\sigma}_2$ using equation (45) if the functional form of f_1^i is known.

6.2 Validity of the Criterion

Equation (52) is valid only when (a) $\bar{r}_2 \approx \bar{r}_1 \gg (\bar{r}_2 - \bar{r}_1)$, (b) $\mathcal{C}_1 \gg |\mathcal{C}_2 + \mathcal{C}_3|$, i.e., the inter-bilayer interaction is negligible, and (c) the $\mathcal{O}(\delta_2^2)$ terms of (45) can be ignored. Condition (a) is obviously met by the numerical example given below (52). Intuitively, condition (b) would be satisfied if the bilayer tension $\bar{\sigma}_2$ is sufficiently large. For a straight two-bilayer myelin, $\bar{\sigma}_2$ is balanced by the net pressure difference Δp across the outer bilayer cylinder (28): $\bar{\sigma}_2 = \bar{r}_2 \Delta p \approx \bar{r}_2 (dp_2^w + \bar{p}_1)$, where \bar{p}_1 (38) represents the strength of the inter-bilayer interaction. This force balance equation implies that $\bar{\sigma}_2$ increases with \bar{r}_2 or Δp . Because \bar{p}_1 (> 0) tends to decrease as $\bar{\sigma}_2$ increases, we expect a sufficiently large \bar{r}_2 or dp_2^w would yield a $\bar{\sigma}_2$ large enough

so that the inter-bilayer interaction can be neglected. In the following we will examine closely whether conditions (b) and (c) are satisfied by the example below (52). Our strategy is to compare the orders of magnitude of the terms of interest.

Equations (32) and (33) with $\delta_{\text{th}} \approx -0.02 \text{ \AA}$ yield

$$\frac{|\delta_{\text{th}}|}{R_1} \sim \frac{\delta d_1}{R_1} \sim \frac{\delta A_2}{A_2} \sim 10^{-7}. \quad (53)$$

Here the use of symbol “ \sim ” means we are only interested in the orders of magnitude of the terms on its both sides. The above equation in turn implies that the $\mathcal{O}(\delta_2^2)$ terms in δd_1 (32) are negligible. Experimental results suggest that the bilayer tension varies linearly with the fractional change in bilayer area when it is sufficiently large (≥ 0.5 dyne/cm for typical lipid bilayers) [25, 26]. Thus, in our case

$$\left(\frac{\partial \sigma_2}{\partial A_2} \right)_i \bar{A}_2 \approx K_A, \quad (54)$$

where K_A is the area compressibility modulus of the bilayer. For typical lipid bilayer membranes, $K_A \approx 200$ dyne/cm [25]. Equations (39) and (54) imply that the fractional change in σ_2 is also small:

$$\frac{\delta \sigma_2}{\bar{\sigma}_2} \approx \frac{K_A}{\bar{\sigma}_2} \frac{\delta A_2}{A_2} \sim 10^{-5}, \quad (55)$$

where $\bar{\sigma}_2 = 2$ dyne/cm. By virtue of (53) and (54), it is straightforward to show that in δF^e (36), the $\mathcal{O}(\delta_2^2/R_1^2)$ term is much less than the $\mathcal{O}(\delta_2/R_1)$ term and thus can be ignored.

The change in the inter-bilayer interaction potential f_1^i reads (see (25) and (37))

$$\delta f_1^i = \sum_{k=2}^6 \mathcal{D}_k + \mathcal{O}\left(\frac{\delta_2^3}{R_1^3}, \delta_2^6\right), \quad (56)$$

where, with (27) and (38),

$$\begin{aligned}
\mathcal{D}_2 &= -\bar{p}_1 \delta d_1, \\
\mathcal{D}_3 &= \left(\frac{\partial f_1^i}{\partial \sigma_2} \right)_i \delta \sigma_2, \\
\mathcal{D}_4 &= \left(\frac{\partial^2 f_1^i}{\partial \sigma_2^2} \right)_i \frac{\delta \sigma_2^2}{2}, \\
\mathcal{D}_5 &= - \left(\frac{\partial p_1}{\partial d_1} \right)_i \frac{\delta d_1^2}{2}, \\
\mathcal{D}_6 &= - \left(\frac{\partial p_1}{\partial \sigma_2} \right)_i \delta d_1 \delta \sigma_2,
\end{aligned}$$

and $\delta d_1 \sim |\delta_{\text{th}}| \approx 0.02 \text{ \AA}$ in our case. The first-order terms \mathcal{D}_2 and \mathcal{D}_3 lead to \mathcal{C}_2 (47) and \mathcal{C}_3 (48), respectively (see (37)). The second-order terms \mathcal{D}_4 , \mathcal{D}_5 , and \mathcal{D}_6 contribute to the $\mathcal{O}(\delta_2^2)$ terms in (45). In our case $\mathcal{C}_1 \approx 2$ erg/cm² (46) is certainly much larger than $\mathcal{C}_2 = 2.4 \times 10^{-4}$ erg/cm²

(47) because $\bar{r}_2 \gg (\bar{r}_2 - \bar{r}_1)$ and $\bar{\sigma}_2 \approx \bar{r}_2 \bar{p}_1$ (28). Therefore \mathcal{C}_2 and \mathcal{D}_2 can be neglected. Besides, we expect that

$$f_1^i \sim p_1 \lambda \quad \text{and} \quad \left(\frac{\partial p_1}{\partial d_1} \right)_i \sim \frac{p_1}{\lambda}, \quad (57)$$

where the length λ can be as small as the decay length ($2 - 3 \text{ \AA}$) of hydration pressure [27] or as large as the inter-bilayer spacing (several nanometers) if the Helfrich repulsion [28] dominates. This means in our case

$$\frac{\delta d_1}{\lambda} \sim \frac{|\delta_{\text{th}}|}{\lambda} \sim 10^{-3} - 10^{-2} \ll 1 \quad (58)$$

and $|\delta_{\text{th}}| \mathcal{C}_1 / R_1 \sim 10^{-7} \text{ dyne/cm}$ is much larger than $\mathcal{D}_5 \sim \mathcal{C}_5 \delta_{\text{th}}^2 \sim 10^{-9} \text{ dyne/cm}$ (see (45)). Hence we can ignore those $\mathcal{O}(\delta_2^2)$ terms of (45) arising from \mathcal{D}_5 . The functional dependence of f_1^i on σ_2 is necessary in order to decide whether \mathcal{D}_3 , \mathcal{D}_4 , and \mathcal{D}_6 are negligible. To go further, we consider two extreme situations. The actual $f_1^i(\sigma_2)$ is expected to fall in between these two extremes.

In the first extreme situation, we assume σ_2 is large enough so that the bilayer thermal undulations [19] can be ignored. This assumption implies that σ_2 is coupled with f_1^i mainly via surfactant number density ρ_s (number of surfactant molecules per unit bilayer area) of the outer bilayer. Intuitively, when σ_2 is sufficiently large (close to the lysis tension) [25], f_1^i should be roughly proportional to ρ_s . With fixed inter-bilayer spacing d_1 (see (56)), equations (55), (57), and the assumption of $f_1^i \propto \rho_s$ lead to

$$\frac{\delta p_1}{p_1} \sim \frac{\delta f_1^i}{f_1^i} \sim -\frac{\delta A_2}{A_2} \approx -\frac{\sigma_2}{K_A} \frac{\delta \sigma_2}{\sigma_2} \quad (59)$$

and thus

$$\frac{\partial f_1^i}{\partial \sigma_2} \approx \frac{\delta f_1^i}{\delta \sigma_2} = -Y \frac{f_1^i}{\sigma_2}, \quad (60)$$

where

$$Y = -\frac{\delta f_1^i / f_1^i}{\delta \sigma_2 / \sigma_2} \approx -\frac{\delta f_1^i / f_1^i}{\delta A_2 / A_2} \frac{\sigma_2}{K_A} \sim \frac{\sigma_2}{K_A}. \quad (61)$$

In our case $\sigma_2 = 2 \text{ dyne/cm}$, $K_A \approx 200 \text{ dyne/cm}$, and hence $Y \sim 10^{-2}$. By use of (57), (59), and (60), we can rewrite \mathcal{D}_3 , \mathcal{D}_4 , and \mathcal{D}_6 :

$$\begin{aligned} \mathcal{D}_3 &= \delta f_1^i \approx -Y f_1^i \left(\frac{\delta \sigma_2}{\bar{\sigma}_2} \right) \sim Y \bar{p}_1 \lambda \left(\frac{\delta \sigma_2}{\bar{\sigma}_2} \right). \\ \mathcal{D}_4 &= \delta \left(\frac{\partial f_1^i}{\partial \sigma_2} \right) \frac{\delta \sigma_2}{2} \sim Y \delta \left(\frac{f_1^i}{\sigma_2} \right) \delta \sigma_2 \\ &\sim Y(Y-1) \bar{p}_1 \lambda \left(\frac{\delta \sigma_2}{\bar{\sigma}_2} \right)^2. \\ \mathcal{D}_6 &= -\delta p_1 \delta d_1 \sim \left(\frac{\delta p_1}{p_1} \right) \left(\frac{\delta d_1}{\lambda} \right) \bar{p}_1 \lambda \\ &\sim Y \bar{p}_1 \lambda \left(\frac{\delta \sigma_2}{\bar{\sigma}_2} \right) \left(\frac{\delta d_1}{\lambda} \right). \end{aligned}$$

Given $Y \sim 10^{-2}$, $\bar{\sigma}_2 \approx 2 \text{ dyne/cm}$, $K_A \approx 200 \text{ dyne/cm}$, $\bar{p}_1 = 10^3 \text{ dyne/cm}^2$, and $\lambda \sim 1 \text{ nm}$, equations (36), (55), and (58) imply

$$\frac{|\delta F^e|}{A_2} = \frac{\bar{\sigma}_2 |\delta A_2|}{A_2} \approx \frac{\bar{\sigma}_2^2 |\delta \sigma_2|}{K_A \bar{\sigma}_2} \gg |\mathcal{D}_3| \gg |\mathcal{D}_4| \text{ or } |\mathcal{D}_6|.$$

Therefore, \mathcal{C}_3 (48), which arises from \mathcal{D}_3 , as well as those $\mathcal{O}(\delta_2^2)$ terms of (45) contributed by \mathcal{D}_4 and \mathcal{D}_6 are negligible in the example below (52). We also note that with (48), (54), (57), (60), and (61),

$$\begin{aligned} \mathcal{C}_3 &\approx \left(\frac{\partial f_1^i}{\partial \sigma_2} \right)_i K_A \approx -Y \frac{f_1^i}{\bar{\sigma}_2} K_A \sim -Y K_A \frac{\bar{p}_1 \lambda}{\bar{\sigma}_2} \\ &\sim -\bar{p}_1 \lambda \sim 10^{-5} - 10^{-4} \text{ erg/cm}^2, \end{aligned}$$

which has approximately the same order of magnitude as $\mathcal{C}_2 = 2.4 \times 10^{-4} \text{ erg/cm}^2$ (47). This means in our case coiling might even lead to $(\mathcal{C}_2 + \mathcal{C}_3) > 0$, i.e., a decrease in the inter-bilayer interaction F^i (see (40), (45), (50), and the text below (49)).

Now we consider the other extreme situation: the dependence of f_1^i on $\bar{\sigma}_2$ originates from bilayer thermal undulations [19, 30, 31]. Here we adopt the functional form derived by Seifert (Eq. (9) of [30]) and express f_1^i as

$$f_1^i = \hat{f}_1^i(\bar{d}_1) + \frac{6b^2 T^2}{\kappa \bar{d}_1^2} \frac{y^2}{\sinh^2(y)}, \quad (62)$$

where $b = 0.1$, $\bar{d}_1 = (\bar{r}_2 - \bar{r}_1)$, and $y = (\bar{\sigma}_2 / bT)^{1/2} \bar{d}_1 / 2$. The term \hat{f}_1^i is the part of f_1^i that is independent of $\bar{\sigma}_2$. The last term is just the Helfrich potential with variable membrane tension. The dependence on $\bar{\sigma}_1$ is neglected because $\bar{\sigma}_1$ is unchanged in the two-step deformation. With (62) and the parameters given below (52), straightforward calculations show that $\mathcal{C}_1 \approx 2 \text{ erg/cm}^2$ (46) is much larger than $|\mathcal{C}_3| \approx 0.04 \text{ erg/cm}^2$ (48) and that both \mathcal{D}_4 and \mathcal{D}_6 are much less than \mathcal{D}_3 . Therefore, \mathcal{C}_3 as well as the $\mathcal{O}(\delta_2^2)$ terms of (45) associated with \mathcal{D}_4 and \mathcal{D}_6 are negligible.

In the previous subsection we use equation (52) to investigate the coiling instability of a two-bilayer myelin (see (51)). This equation is valid only when (a) $\bar{r}_2 \approx \bar{r}_1 \gg (\bar{r}_2 - \bar{r}_1)$, (b) $\mathcal{C}_1 \gg |\mathcal{C}_2 + \mathcal{C}_3|$, i.e., the inter-bilayer interaction is negligible, and (c) the $\mathcal{O}(\delta_2^2)$ terms in (45) can be ignored. We are interested in the example described below (52), which clearly satisfies condition (a). In this subsection we examine conditions (b) and (c) by estimating the orders of magnitude of the relevant terms. We show that these two conditions are also satisfied. Thus, equation (52) is indeed applicable to the case of interest.

6.3 Generalization for Multiple-bilayer Myelins

In principle the results of Section 6.1 can be applied to myelins of multiple bilayers. This is because in terms of

energy (see (17) and (41)), an N -bilayer myelin can be decomposed into $(N - 1)$ nested two-bilayer myelins. Although the bilayer tension σ_n (22) may vary from bilayer to bilayer, equation (41) implies that the coiled state is still favorable as long as the net decrease in F^e is larger than the net increase in $F^c + F^i$.

Equation (41) and its implications for myelin coiling can also be understood with a gedanken experiment, where a multiple-bilayer myelin is constructed from two-bilayer myelins. We take the numerical example below (52) as our initial two-bilayer myelin. The bending curvature $1/R_1$ and the eccentricity δ_2 are allowed to vary freely so that the myelin is in equilibrium. The equilibrium state has a finite R_1 and a δ_2 of magnitude larger than $|\delta_{\text{th}}|$ ($\approx 0.02\text{\AA}$). This means δF (45) is less than zero. Put it in another way, the two-step deformation (Fig. 8) produces a surplus of energy. Since $|\delta_{\text{th}}|$ of this initial myelin is quite small, the equilibrium value of $|\delta_2|$ is expected to be much larger than $|\delta_{\text{th}}|$. Therefore the energy surplus $|\delta F|$ should also be much larger than the curvature energy cost of coiling δF^c (34). We keep R_1 unchanged and insert another two-bilayer myelin into the inside of the initial one. Now the system becomes a four-bilayer myelin. The energy surplus $|\delta F|$ may increase or decrease as a result of this new addition. We can repeat this process and add more two-bilayer myelins to the system as long as the energy surplus is not depleted, i.e., δF is still less than zero. Even when $\delta F > 0$, we can increase the bilayer tensions in those existing two-bilayer myelins so that δF becomes negative again. The above gedanken experiment shows clearly that a multi-bilayer myelin can coil to lower its energy when the bilayer tension is sufficiently large.

Let us consider the case depicted by Figure 2b. In this case the material influx density for the core is increasingly greater than that for the shell. Eventually the bilayer tension in the shell will be large enough to cause the myelin to bend or coil. To be more specific, the free energy analysis (41) can be done in the following manner. First, the eccentricities δ_n (Fig. 5) of the bilayers in the core are artificially constrained to be zero, while those in the shell are free to vary. We start with state (i) (Fig. 8), i.e., $R_1 \rightarrow \infty$ and $\delta_n = 0$ for all n . By symmetry state (i) is the equilibrium configuration for straight myelins. Secondly, we perform the two-step deformation (Fig. 8) and allow the system to reach equilibrium at finite R_1 . This means those variable eccentricities δ_n are at the values minimizing the total energy F (17). Because every δ_n in the core is set to zero, the deformation of the core only costs curvature energy (34). Previous analysis of the two-bilayer myelin suggests that when the bilayer tensions σ_n in the shell are large enough, the two-step deformation would lead to a net decrease in F and thus state (iii) becomes energetically favorable. Lastly, the constraint of $\delta_n = 0$ in the core is dismissed and the system is allowed to equilibrate again. Obviously, if state (iii) has been more stable than state (i)

as a result of large bilayer tension in the shell, it would be still favorable because the new degrees of freedom would only lower the total energy F further. Therefore, we conclude that the myelin of Figure 2b would bend or coil when the bilayer tension in the shell is sufficiently large. In the sense of coarse-graining, this case can be treated as a “two-bilayer” myelin, whose inner and outer bilayers correspond to the core and the shell, respectively.

7 Discussion

Our model predicts that a sufficiently large bilayer tension may cause a myelin to coil. The coiling mechanism is explained with the two-bilayer case studied in detail in the previous section. In the following we will discuss the experimental techniques that might be used to test our model. We will also look into some important features as well as implications of our model.

In order to test the proposed model of myelin coiling, one needs to be able to either measure or manipulate the bilayer tension of a myelin. Optical tweezers may be a promising tool [32, 33]. When a bilayer is optically tweezered, surfactant molecules are pulled into the trap set by the tweezers and thus the bilayer tension increases. An advantage of optical tweezers is that they can penetrate into a myelin and grab multiple bilayers. However, laser-induced tension is usually weak ($10^{-3} - 10^{-2}$ dyne/cm) [34]. It remains a question whether such a weak tension can induce myelin coiling. Another method is micropipet suction [25, 26]. In contrast to optical tweezers, this method can produce a bilayer tension as large as the lysis tension [25]. Nonetheless, it can be applied only from the outside of a myelin. Although suction of a myelin with a micropipet is an interesting problem in its own right, whether it can cause myelin coiling is still uncertain.

The second constraint described in Section 4.3 requires volume conservation for each bilayer cylinder. It should be a fair condition for defect-free myelins [35] since water permeabilities of typical lipid bilayers are quite small [16, 36]. This constraint is also necessary in our model because it eliminates a potential inconsistency between properties (a) and (b) described in Section 4.3: if bilayers can exchange material, a nonuniform bilayer tension may induce a sufficiently large material flow between bilayers to relax the tension that drives coiling.

For simplicity the spontaneous curvature K_0 (18) is set to zero in this work. A nonzero or nonuniform K_0 would only alter the curvature energy F^c (20) by some finite amount and therefore does not weaken the proposed coiling mechanism at all [13, 17]. In addition, the cross sections of the bilayer cylinders are assumed to be circular (Fig. 5). Although this might be a fair assumption for straight myelins, there is no reason why this is still the case for coiled myelins. Because δ_n is in general nonzero in state (iii) (Fig. 8), the shape of the cross section should change

accordingly. However, allowing this to happen would only lower the energy of a coiled myelin further (cf. (41)) and thus would not render our model invalid.

The myelin free energy F (17) is the sum of the curvature energy F^c , the elastic energy F^e of bilayer tension, and the inter-bilayer interaction energy F^i . Because F^c is known (20), determining the change in F^c due to coiling is straightforward (34). The change in F^e , to lowest order, is given by $\sum \bar{\sigma}_n \delta A_n$, where $\bar{\sigma}_n$ is taken as an independent parameter (see (36)). Thus, direct knowledge of F^e is not crucial for studying myelin coiling at the level of this work. This, however, is not the case for F^i (24). In order to analyze the coiling instability in detail, the functional form of f_n^i (25) is required even though we have shown that its contributions can be neglected under certain conditions (Sect. 6). Yet, to our knowledge, the complete functional expression of f_n^i is still not known. Therefore more investigations of f_n^i are needed. In the context of this work, f_n^i has to satisfy the force balance equation (28).

In the example below (52) we use a small inter-bilayer pressure ($\bar{p}_1 = 10^3$ dyne/cm²) while our previous work [16] suggests that the inter-bilayer pressure (27) in a multi-bilayer myelin is, on the average, larger than this value. This, however, is not a contradiction. In view of equation (28), a two-bilayer myelin with $\sigma_2 = 2$ dyne/cm, $r_2 = 20$ μm , and $dp_n^w = 0$ dyne/cm² must have an inter-bilayer pressure of about 10^3 dyne/cm². As for myelins composed of multiple bilayers, equation (28) also allows a much larger inter-bilayer pressure p_n , provided that the net pressure difference ($dp_n^w + p_{n-1} - p_n$) yields a reasonable bilayer tension σ_n . Thus, a multi-bilayer myelin may have a large inter-bilayer pressure p_n as long as the net pressure gradient across the bilayers is small. This leads to an interesting question in the physics of myelins: what determines the width (diameter) of myelins? Our model suggests bilayer tension may be an important factor. As just mentioned, an inter-bilayer pressure of 10^3 dyne/cm² ($\approx 10^{-3}$ atm) with a radius of 20 μm yields a bilayer tension of 2 dyne/cm, which is close to the lysis tension of lipid bilayer membranes ($1 - 20$ dyne/cm) [25]. In contact experiments myelins of diameter $10 - 50$ μm form immediately after bulk surfactant is contacted with water (Sect. 2) [6, 7, 8]. The surfactant concentration at the contact interface should be sufficiently high so that the inter-bilayer interaction is repulsive. Therefore, even in view of the complex kinetics of surfactant dissolution [37], an obvious upper bound for myelin diameter is prescribed by the lysis tension of the bilayer and the outermost inter-bilayer pressure in myelins. By the same token, we can estimate the outermost inter-bilayer pressure using the observed myelin diameter and lysis tension.

8 Conclusions

In this work we propose a model to explain coiling of myelins often seen in contact experiments. This model has two important features: the constituent bilayer cylinders of a myelin can be non-coaxial and the bilayer tension can vary from bilayer to bilayer. The analysis indicates the importance of bilayer tension in determining the morphology of a myelin: a myelin can coil if the bilayer tension is large enough. The coiling mechanism is in a sense similar to the classical Euler buckling of a thin elastic rod subject to axial compression [20].

Our model suggests that myelins have complex internal structures. The internal stresses such as bilayer lateral tension may be very different for seemingly like myelins. As a result, our model should not be deemed inconsistent with other models [12, 13, 17]. On the contrary, the existence of all these models, including ours, reflects the complexity of myelinic structures and suggests multiple routes to myelin coiling. However, the following questions are also legitimate. Is our model applicable to the systems that were previously explained with different models [10, 12, 13]? If so, how can we determine which model better explains the experimental results? Moreover, owing to the complexity of myelins, experimentalists are faced with a serious challenge: how can one produce myelins in a controllable fashion? To answer these questions, more experimental as well as theoretical investigations are needed.

This work is done as part of the author's doctoral research under the supervision of Prof. Thomas A. Witten. The author thanks Prof. Witten for his generous support and countless inspiring discussions. The author also appreciates many useful comments from Ling-Nan Zou and Prof. Sidney R. Nagel. This work was supported in part by the MRSEC Program of the National Science Foundation under Award Number DMR-0213745.

References

- [1] O.G. Mouritsen, *Life - As a Matter of Fat: The Emerging Science of Lipidomics* (Springer, Berlin, 2005)
- [2] J.N. Israelachvili, *Intermolecular and Surface Forces*, 2nd edn. (Academic Press, San Diego, 1998)
- [3] R.G. Laughlin, *The Aqueous Phase Behavior of Surfactants* (Academic Press, San Diego, 1996)
- [4] W. Harbich, W. Helfrich, *Chem. Phys. Lipids* **36**, 39 (1984)
- [5] W.J. Benton, K.H. Raney, C.A. Miller, *J. Colloid Interface Sci.* **110**, 363 (1986)
- [6] I. Sakurai, T. Suzuki, S. Sakurai, *Mol. Cryst. Liq. Cryst.* **180B**, 305 (1990)

- [7] M. Buchanan, S.U. Egelhaaf, M.E. Cates, *Langmuir* **16**, 3718 (2000)
- [8] M. Haran, A. Chowdhury, C. Manohar, J. Bellare, *Colloids Surf. A* **205**, 21 (2002)
- [9] L.-N. Zou, S.R. Nagel, <http://arxiv.org/abs/cond-mat/0509740>
- [10] K.-C. Lin, R.M. Weis, H.M. McConnell, *Nature* **296**, 164 (1982)
- [11] I. Sakurai et al., *Mol. Cryst. Liq. Cryst.* **130**, 203 (1985)
- [12] K. Mishima, K. Fukuda, K. Suzuki, *Biochim. Biophys. Acta* **1108**, 115 (1992)
- [13] V. Frette et al., *Phys. Rev. Lett.* **83**, 2465 (1999); I. Tsafrir et al., *Phys. Rev. E* **63**, 031603 (2001)
- [14] H. Dave, M. Surve, C. Manohar, J. Bellare, *J. Colloid Interface Sci.* **264**, 76 (2003)
- [15] D.D. Lasic, *Liposomes: From Physics to Applications* (Elsevier, Amsterdam, 1993)
- [16] J.-R. Huang, L.-N. Zou, T.A. Witten, *Eur. Phys. J. E* (to be published) DOI: 10.1140/epje/e2005-00035-8
- [17] C.D. Santangelo, P. Pincus, *Phys. Rev. E* **66**, 061501 (2002)
- [18] E. Evans, R. Skalak, *Mechanics and Thermodynamics of Biomembranes* (CRC Press, Boca Raton, 1980)
- [19] W. Helfrich, R.-M. Servuss, *Nuovo Cimento D* **3**, 137 (1984)
- [20] A.E.H. Love, *A Treatise on the Mathematical Theory of Elasticity*, 4th edn. (Dover, New York, 1944)
- [21] K. Mishima, K. Yoshiyama, *Biochim. Biophys. Acta* **904**, 149 (1987)
- [22] A. Sein, J.B.F.N. Engberts, *Langmuir* **12**, 2924 (1996)
- [23] T.A. Witten, *Structured Fluids: Polymers, Colloids, Surfactants* (Oxford University Press, New York, 2004)
- [24] D.J. Struik, *Lectures on Classical Differential Geometry*, 2nd edn. (Dover, New York, 1988)
- [25] E. Evans, D. Needham, *J. Phys. Chem.* **91**, 4219 (1987)
- [26] E. Evans, W. Rawicz *Phys. Rev. Lett.* **64**, 2094 (1990)
- [27] R.P. Rand, V.A. Parsegian, *Biochim. Biophys. Acta* **988**, 351 (1989)
- [28] W. Helfrich, *Z. Naturforsch.* **33a**, 305 (1978)
- [29] H. Diamant, M.E. Cates, *Eur. Phys. J. E* **4**, 223 (2001)
- [30] U. Seifert, *Phys. Rev. Lett.* **74**, 5060 (1995)
- [31] R.R. Netz, R. Lipowsky, *Europhys. Lett.* **29**, 345 (1995)
- [32] R. Bar-Ziv, E. Moses, *Phys. Rev. Lett.* **73**, 1392 (1994)
- [33] J.E. Curtis, B.A. Koss, D.G. Grier, *Opt. Commun.* **207**, 169 (2002)
- [34] R. Bar-Ziv, E. Moses, P. Nelson, *Biophys. J.* **75**, 294 (1998)
- [35] M. Kléman, *Points, Lines and Walls: In Liquid Crystals, Magnetic Systems and Various Ordered Media* (John Wiley & Sons, New York, 1983)
- [36] S.-J. Marrink, H.J.C. Berendsen, *J. Phys. Chem.* **98**, 4155 (1994)
- [37] P.B. Warren, M. Buchanan, *Curr. Opin. Colloid Interface Sci.* **6**, 287 (2001)